Journal of Alloys and Compounds 1036 (2025) 181844

Contents lists available at ScienceDirect

Journal of Alloys and Compounds

journal homepage: www.elsevier.com/locate/jalcom

Research article

In-situ temperature calibration for high temperature XRD experiments in vacuum demonstrated on pristine and Nb doped TiO_{2-x} thin films

David Freudenblum [a,*], Gaston Gruber [a], René Schwiddessen [c], Florian Ruske [b], Nikolaus Weinberger [a]

[a] University of Innsbruck, Department of Structural Engineering and Material Science, Technikerstrasse 13, Innsbruck, 6020, Austria
[b] Helmholtz-Centre Berlin, Kekuléstraße 5, Berlin, 12489, Germany
[c] Helmholtz-Centre Berlin, Department Structure and Dynamics of Energy Materials, Berlin, 12489, Germany

ARTICLE INFO

Keywords:
In-situ high temperature XRD
In-situ temperature calibration
DC magnetron sputtering
Niobium doped titanium dioxide
Thin films

ABSTRACT

We present an *in-situ* temperature calibration technique for high temperature grazing incident X-ray diffraction experiments conducted in high-vacuum. Thermal lattice extension of a crystalline platinum thin film is used to calibrate the temperature in the sample to the control-temperature measured by a thermocouple. This enables a precise thermal analysis of thin film crystal structures with an uncertainty of less than 10 K. Using this technique, we examine the crystallization behavior of pristine and niobium-doped titanium dioxide thin films, deposited by direct current magnetron sputtering from metal–ceramic composite targets. Crystallization onset temperatures and structural evolution were assessed for various target compositions and process conditions, revealing that increased metal content in the composite target tends to promote rutile phase formation during vacuum annealing. For the target containing 10^{wt}% niobium – identified as the most promising for a transparent conductive oxide application – an oxygen flow variation is evaluated. Results reveal significant differences in the crystal lattice depending on the oxygen flow during deposition. Introducing 0.2 % oxygen to the argon process gas is sufficient to induce the formation of pure anatase phase during heat treatment, yielding a minimum resistivity of 1.2 m Ω cm. Our findings highlight the crucial role of oxygen content in tailoring both the structural and opto-electrical properties of titanium dioxide based thin films, providing essential insights for the definition of optimal process windows.

1. Introduction

In high-temperature (HT) X-ray diffraction (XRD) experiments conducted in non ambient environment, a precise calibration of temperature is often challenging. The difference between the actual temperature in the specimen and the measured temperature to control the experiment has to be calibrated. Commonly, a thermocouple, welded to the underside of the heating stripe or in direct contact with the specimen is used to control the temperature. Calibration is performed using either a single-point calibration material (phase transition standard) or a multi-point calibration standard, where accurately known thermal expansion data provides a calibration curve [1]. The position and the quality of thermal contact of the thermocouple is decisive for the accuracy of the calibration [2]. In many experiments, a direct contact to the specimen is not, or only insufficiently possible, and hence it remains a thermocouple mounted to the heating stripe. In ambient environment and for small samples placed directly on the heating stripe, the calibration of a thermocouple mounted on the underside of the heating stripe might be sufficient, but when vacuum conditions are present, the calibration will get invalid. In vacuum, heat transfer is dominated by thermal radiation, which can lead to significant temperature aberrations in the specimen. Substrate materials in thin film applications can cause additional heat loss depending on e.g. thermal conductivity and thickness, leading to a further decrease in the actual substrate temperature. Hence, the choice of substrate material has a direct effect on the real temperature in the sample thin film. Classical calibration methods using bulk or powder standard materials are not sufficient to capture the true thermal conditions of the thin film in vacuum, as they do not account for the complex thermal decoupling between heater and sample, especially in radiative regimes. The emissivity and thermal mass of thin film/substrate stacks differ substantially from those of typical calibration materials, rendering ex-situ calibration with conventional standards inaccurate. Here we report a method for in-situ temperature calibration in thin film applications. We use the thermal extension of lattice spacing in a polycrystalline platinum (Pt) thin film.

* Corresponding author.
E-mail address: david.freudenblum@uibk.ac.at (D. Freudenblum).

https://doi.org/10.1016/j.jallcom.2025.181844
Received 3 April 2025; Received in revised form 15 June 2025; Accepted 24 June 2025
Available online 8 July 2025

A thin film of interest deposited on top of the Pt film can be investigated by grazing incident (GI-) XRD. When the angle of incident is adjusted in a way that both films can be probed, the Pt reflection can be used to calibrate the temperature in the actual sample thin film. A preliminary stage of our presented technique is used in [3], where a Pt foil is placed on the substrate and the temperature is calibrated ex-situ before investigating the actual specimen. Our approach, in contrast, provides a direct and geometry-specific measure of the local sample temperature, enabling improved accuracy and reproducibility in structural studies under vacuum conditions. The application of our technique is demonstrated by investigating the crystallization of doped and undoped TiO_{2-x} thin films deposited by direct current (DC) magnetron sputtering.

TiO_2 based thin films have an extraordinarily broad variety of applications, such as photocatalysis [4], thermoelectric devices [5] or opto-electronic devices like thin film photovoltaic cells. The desired properties for each application are accordingly manifold. Likewise, there are many approaches to optimize material properties for desired application, by doping or different synthesis condition and techniques. We will focus on compact TiO_2 films, which can be used in photovoltaic devices as electron transport layer [6–8], buffer [9] or passivation layer [10]. Niobium (Nb) doped TiO_2 deposited on single crystal substrates by pulsed laser deposition (PLD) was initially discovered as a very promising transparent conductive oxide (TCO) material in [11] and has since been subject to extensive research.

Another approach is the deposition via magnetron sputtering, which is particularly interesting for large scale industrial production as magnetron sputtering is a well established, robust and an easy scalable process. TiO_2 is a non conductive ceramic material, and subsequently requires radio frequency (RF) sputtering. However, if slightly reduced TiO_{2-x} or composite Ti–TiO_2 targets are used, DC sputtering is possible [12]. Apart from that, the films can be prepared by reactive sputtering from metallic targets. Operating in such an oxidic sputter mode significantly drops the deposition rate and leads to issues with a well known hysteresis effect caused by compound formation on the target [13–15]. Further, this has certainly one major disadvantage, especially when not fully stoichiometric thin films are required. To produce TCO like properties, the films must be deposited in an unstable regime between metallic and oxidic sputter mode and therefore, a precise active oxygen partial pressure control is crucial [16]. In [17], discharge voltage was adjusted to control the sputter mode with constant oxygen flow. Our approach is the use of conductive metal–TiO_{2-x} composite targets, which not only allows for DC sputtering in a quasi-metallic mode, but also enables a way of doping the thin films with reasonable deposition rates.

For PV applications, electro-optical properties are decisive, which are strongly correlated with crystal structure and certain doping concentrations. As-deposited thin films are often amorphous or nanocrystalline and develop crystalline phases only after thermal treatment. In this study, we investigate the crystallization of pristine and doped TiO_2 based thin films prepared by DC magnetron sputtering from composite targets by in-situ high temperature grazing incident (GI-)XRD in vacuum environment. Correlations of opto-electrical properties and crystal structure of the thin films are studied.

2. Experimental and methods

2.1. Thin film fabrication and characterization

The investigated thin films, including Pt and TiO_{2-x} based ones, are deposited in a modified EDWARDS Auto 306 sputter coater, equipped with two planar circular magnetrons. Four sample/substrate holders can be mounted, which are rotating in a planetary movement 50 mm (adjustable) above the target surface. Generally, the pre-process vacuum is maintained below $2{\cdot}10^{-4}$ Pa before the process gas is introduced. The Pt thin films are sputtered from a Pt (99.99%) sputter target provided by *Sindlhauser GmbH* with a diameter of 7.6 cm and a thickness of 3 mm.

We select fused silica substrates for their excellent temperature stability in the investigated range. To mitigate the risk of thin film delamination due to thermal stress during high-temperature experiments, we roughen the substrates by milling the surface with 9 µm suspension (*Struers MD Largo* grinding surface and *DiaPro Plan 9* µm diamond suspension). The substrates, each with a thickness of 2 mm, are cut into 50 mm × 50 mm sheets, thoroughly roughened, cleaned, and subsequently coated with a 300 nm layer of Pt (referred to as $Pt^{300\,nm}$). For the fabrication of $Pt^{300\,nm}$ films, argon (Ar) process gas is introduced with a constant flow of 68 sccm, resulting in a process pressure of 0.32 Pa. A constant DC power of 200 W (equal to 5.2 W/cm^2) was applied to the magnetron for 340 s. After Pt deposition, the sheets were cut in smaller pieces for further experiments.

Niobium (Nb) doped Titanium oxide (Nb:TiO) and pristine TiO_{2-x} thin films are sputtered from pristine and composite targets produced by *RHP Technology GmbH*. The circular targets with a diameter of 7 cm and a thickness of 3 mm are bonded to a 2 mm thick copper base plate. The detailed sputter conditions are described in Section 2.3 and summarized in Table 1.

GI-XRD is performed with a Panalytical Empyrean equipped with a Cu Kα X-ray source (wavelength 1.54056 Å, powered with 50 kV and 30 mA), an X-ray mirror for parallel optics, and a height adjustable Anton Paar HTK16N heating stage connected to a turbo molecular pumping system. All XRD experiments, including all applied thermal treatments, are generally performed at a pressure lower than $1{\cdot}10^{-2}$ Pa.

Transmission/Reflection experiments are performed with a Perkin Elmer Lambda 1050 with integrating sphere. A calibrated mirror or a spectralon is used as a reflection standard. Ellipsometric spectra are recorded at incident angles of 30, 40, 50, 60 and 70 degree in the spectral region from 190 nm to 2500 nm using a Sentech SE 850 DUV.

Sheet resistance is measured with a Jandel RM3-AR 4-point probe system directly after deposition and again after vacuum heat treatment. The electrical properties of them are further analyzed by Hall effect measurements in the van der Pauw geometry using an Ecopia HMS-3000 system. We use a Rigaku Primus III+ wavelength-dispersive X-ray fluorescence (WD-XRF) setup to measure the composition and thickness of the thin films. Finally, imaging of the thin film micro structure is performed with a Jeol JSM-7610F field emission scanning electron microscope (SEM).

2.2. Temperature calibration using the Pt lattice parameter *a*

The in-situ temperature calibration is performed by assessing thermal expansion of crystal lattice in a platinum thin film via high temperature GI-XRD measurements. GI-XRD experiments are performed with an incident angle (ω) of 2° and a divergence slit of 1/2 °. The lattice expansion is precisely determined by tracking the shift in the XRD reflex peaks, analyzed by Le Bail refinement [18] and Bragg's law. The calibration is done on $Pt^{300\,nm}$ samples deposited on fused silica substrates. To ensure stable crystalline quality, annealing via a thermal pre-treatment at 1273 K for 2 h is applied within the heating stage under high vacuum and screened via GI-XRD. Subsequently, the temperature GI-XRD program is done at set, nominal temperatures (T_{set}): 299 K as well as between 473 K and 973 K in steps of 25 K, furthermore at 1023 K, 1073 K, 1173 K, and finally at 1273 K. For each temperature step the Pt lattice parameter a is extracted by Le Bail refinement. The lattice dilatation $\Delta a = a_{T_{cal}} - a_{T_0}$ with respect to the lattice parameter $a_{T_{cal}}$ at the real, calibrated temperature T_{cal} compared to a_{T_0} at reference temperature (RT) $T_0 = 299$ K obeys the thermal expansion relationship

$$\frac{\Delta a}{a_{T_0}} = \alpha(T_{cal})(T_{cal} - T_0), \tag{1}$$

with the thermal heat expansion coefficient $\alpha(T_{cal})$, which was determined for Pt by [19] and more recently by [20]. Following Eq. (1), the

unknown real temperature T_{cal}, depending on $\alpha(T_{cal})$, is computed using the measured lattice parameter a_{T_0} and $a_{T_{cal}}$ through an iterative least squares method.

It is important to emphasize, that mirror optics is used to parallelize incident beam to assure invariance of the peak position to the exact vertical (z-) position of the specimen in the measurement stage. Without this optical setup, the peaks would additionally shift due to thermal expansion of the heating stripe in the z-direction.

2.3. Crystallization of TiO_{2-x} based thin films

Here, we apply the above described technique for in-situ temperature calibration to TiO_{2-x} based thin films and investigate the crystallization behavior. TiO_{2-x} based thin films are deposited on pre-tempered (1273 K for 2 h) $Pt^{300\ nm}$ coated fused silica substrates (12 mm × 50 mm). In total six M:TiO_{2-x} (M=Ti, Nb) sputter targets with different metallic Nb or Ti content (0 wt% Ti, 5 wt% Ti, 19 wt% Ti, 2 wt% Nb, 5 wt% Nb, and 10 wt% Nb) are used. Hence, we divide the samples into two sets, where one set is doped with Nb and the other one is pristine. The pristine ones are produced either from pure TiO_{2-x} or from Ti–TiO_{2-x} composite targets. From each target, one sample is produced without adding oxygen (O_2) to the Ar process gas and one with an oxygen flow $\mathcal{F}_{O_2} = F_{O_2}/F_{total} = 3\%$ ($F_{O_2} = 2.04$ sccm) during the deposition. Additionally, for the 10 wt% Nb:TiO_{2-x} target, an oxygen flow variation is performed from $\mathcal{F}_{O_2} = 0.2\%$ ($F_{O_2} = 0.14$ sccm) to $\mathcal{F}_{O_2} = 1\%$ ($F_{O_2} = 0.68$ sccm). We use a sample notation like ^{10}NTO-0.4, indicating 10 wt% Nb in the target and 0.4% oxygen ($\mathcal{F}_{O_2}$) in the process gas. TO is used for Ti–TiO_{2-x} composite targets, accordingly. Pre-process conditions and setup were identical to the Pt depositions. The total gas flow is set to $F_{total} = F_{O_2} + F_{Ar} = 68$ sccm and the magnetron is operated with an applied constant 100 W (2.6 W/cm^2) DC power. We adapted the deposition time to get a nominal film thickness of 140 nm, using an approximated deposition rate. The detailed sputter conditions are summarized in Table 1. Subsequently, the samples were investigated by high temperature GI-XRD experiments including in-situ temperature calibration. We choose an incident angle (ω) of 2° and a divergence slit of 1/2° for all measurements. With these settings, we are able to detect both, the Pt calibration layer and the TiO_{2-x} thin film while also reaching a good illumination of the sample with incident X-rays. The heating procedure follows the temperature program outlined in Section 2.2, with diffraction patterns captured at each temperature step. Le Bail refinement of Pt reflexes within each pattern gives the lattice parameter a for each temperature step, which is used to determine thermal expansion and subsequently, to calibrate the temperature. In order to determine crystallization onset, temperature evolution of the TiO_2 reflexes are investigated by evaluating respective change in peak intensities.

2.4. Opto-electrical characterization of TiO_{2-x} based thin films

In this section, we investigate the effect of oxygen content in the process gas on electro-optical properties of ^{10}NTO thin films. Therefore, sheet resistance and Hall measurements, as well as transmission/reflection experiments and spectroscopic ellipsometry are performed for ^{10}NTO samples with different oxygen content during the sputter process. Samples are prepared with the same sputter conditions as for the deposition of corresponding thin films on Pt coated fused silica substrates (see Section 2.3). Here, ^{10}NTO thin films are deposited directly on EAGLE XG (24 mm × 24 × 1.1 mm, *Präzisionsglas Optik GmbH*) glass substrates. The samples are characterized both in their as-deposited state and after vacuum heat treatment under the same conditions as the corresponding Pt-coated samples.

Table 1
Sample overview and sputter conditions for TiO_{2-x} based thin films.

Sample	Target	P W	F_{total} sccm	F_{O_2} sccm	$\mathcal{F}_{O_2}$ %	p Pa	t min
^{0}TO-3	TiO_{2-x}	100	68	2.04	3	0.32	300
^{0}TO-0	TiO_{2-x}	100	68	0	0	0.32	40
^{5}TO-3	$5^{wt\%}$Ti–TiO_{2-x}	100	68	2.04	3	0.32	290
^{5}TO-0	$5^{wt\%}$Ti–TiO_{2-x}	100	68	0	0	0.32	30
^{19}TO-3	$19^{wt\%}$Ti–TiO_{2-x}	100	68	2.04	3	0.32	240
^{19}TO-0	$19^{wt\%}$Ti–TiO_{2-x}	100	68	0	0	0.32	25
^{2}NTO-3	$2^{wt\%}$Nb–TiO_{2-x}	100	68	2.04	3	0.32	136
^{2}NTO-0	$2^{wt\%}$Nb–TiO_{2-x}	100	68	0	0	0.32	23
^{5}NTO-3	$5^{wt\%}$Nb–TiO_{2-x}	100	68	2.04	3	0.32	122
^{5}NTO-0	$5^{wt\%}$Nb–TiO_{2-x}	100	68	0	0	0.32	19
^{10}NTO-3	$10^{wt\%}$Nb–TiO_{2-x}	100	68	2.04	3	0.32	95
^{10}NTO-1	$10^{wt\%}$Nb–TiO_{2-x}	100	68	0.68	1	0.32	35
^{10}NTO-0.6	$10^{wt\%}$Nb–TiO_{2-x}	100	68	0.41	0.6	0.32	26
^{10}NTO-0.4	$10^{wt\%}$Nb–TiO_{2-x}	100	68	0.27	0.4	0.32	20
^{10}NTO-0.2	$10^{wt\%}$Nb–TiO_{2-x}	100	68	0.14	0.2	0.32	17
^{10}NTO-0	$10^{wt\%}$Nb–TiO_{2-x}	100	68	0	0	0.32	12

3. Results and discussion

3.1. Temperature calibration

The initial reference XRD measurement at $T_0 = 299$ K of a pre-tempered $Pt^{300\,nm}$ is shown in Fig. 1 over the full recorded range of diffraction angles 2Θ. We recognize an elevated intensity of the Pt 111 reflex. It is significantly higher than relative peak intensities of crystallographic information files (CIF) from the Inorganic Crystal Structure Database (ICSD), indicating a preferential orientation. ICSD 243678 [21] is used for Le Bail refinement and yields a lattice parameter $a = 3.924$ Å, microstrain ν of 0.18% and a domain size D larger than the resolution limit of XRD ($D > 130$ nm). The low value of microstrain substantiates that the films are low in defects. The roughened glass surface suppresses potential thermally induced tensions at the glass/Pt interface. Poor adhesion of the Pt films and the consistency with data of bulk lattice parameters suggest that thermally induced macrostrain is insignificant. Due to the fact that the entire diffraction pattern is refined for all investigated temperatures, an-isotropic expansion would be reflected by the extracted parameters and its uncertainty of the refinement. The diffraction patterns in the range of the Pt 111 reflex for each of the five annealing cycles, tempered up to 1273 K, are shown in the inset of Fig. 1. During each cycle, the temperature was ramped up with a rate of 10 K/min starting from T_0 and kept at 1273 K for 10 min, before cooling down to T_0 and recording an XRD pattern. Table 2 lists the peak center positions x_c along with their respective uncertainties, as well as the peak width w of the Kα_1 fits. The peak position shifts to smaller diffraction angles with an increasing number of cycles. Convergence is indicated as between cycle number 4 and 5, the difference in peak position is reduced to 6.9×10^{-4} degree. The reduction of the peak width w implies an improvement of crystalline quality after each cycle or temper time. Therefore, we define the pre-temper time for $Pt^{300\,nm}$ thin films to 2 h. Under these thermal pre-treatment conditions, we achieve a peak center position difference of only 6.2×10^{-4} degree before and after the temperature program. This proofs both the crystalline stability and the reversible thermal expansion behavior of the samples, which are essential requirements for the use as a calibration layer in our application. Taking a closer look at the left shoulder of the Pt 111 peak (see inset in Fig. 1), we recognize two additional features at around 35.8° and 37.9°. These peaks are identified as the copper Kβ_1 respective tungsten Lα_1 wavelength position of the Pt 111 plane. The last mentioned originates from impurities due to the tungsten filament of the X-ray source.

In Fig. 2, the temperature evolution of the Pt 111 reflex from 299 K to 1273 K, with respect to the nominal temperature, is presented. We observe a continuous shift of the peak center x_c to smaller

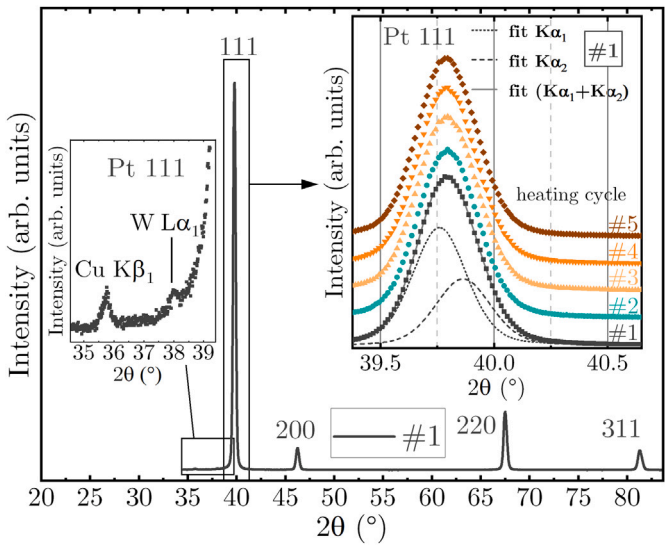

Fig. 1. Reference XRD pattern at RT after pre-temper treatment; insets display a magnification of the left shoulder of Pt 111 reflex and Pt 111 reflection after several heating cycles, respectively.

Table 2
Peak center position x_c with uncertainty and peak width w of the Kα_1 fits in Fig. 1 given in degree.

Cycle	x_c	Error x_c	w
#1	39.76017	±3.5E−4	0.31298
#2	39.75904	±2.7E−4	0.31014
#3	39.75783	±3.0E−4	0.30773
#4	39.75673	±2.6E−4	0.30456
#5	39.75604	±3.0E−4	0.30366

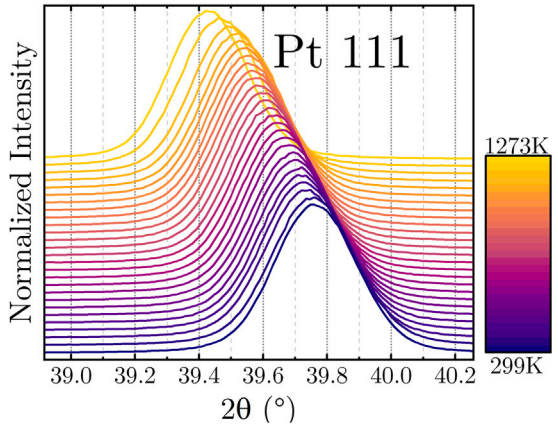

Fig. 2. XRD temperature evolution of Pt 111 reflection from 299 K to 1273 K.

diffraction angles with increasing temperature, which is consistent with an increasing lattice plane distance d and consequently an increased lattice parameter a due to thermal expansion. Based on these resulting differences in lattice parameters Δa, the actual calibrated temperature T_{cal} within the thin film is calculated according to Eq. (1). To further investigate the influence of sample size and positioning of the $Pt^{300\,nm}$ film, five different samples are measured and shown in Fig. 3, illustrating the variations observed as a function of the nominal set temperature T_{set}.

The progression of T_{cal} in Fig. 3 is non-linear, with the difference between nominal and calibrated temperatures increasing at higher values to a maximum of 340 K for the 12 mm × 50 mm sample. A phenomenon influenced by two primary mechanisms that affect the

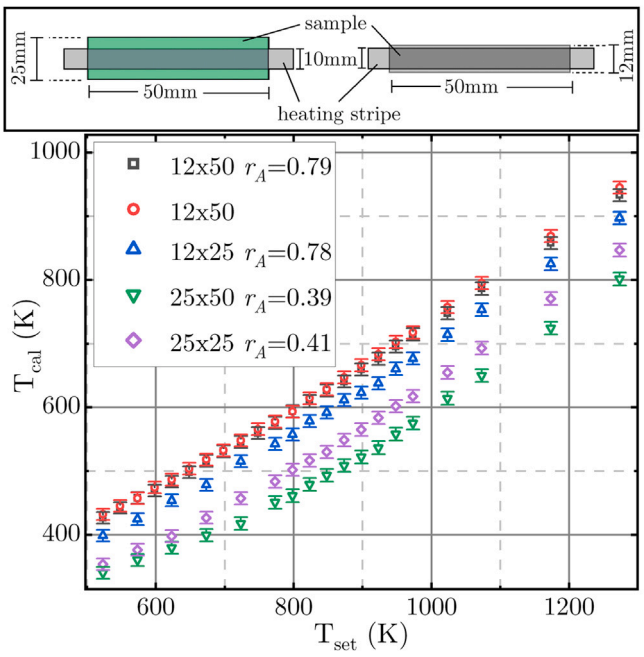

Fig. 3. Calibrated temperature T_{cal} vs. setpoint temperature T_{set} for differently sized $Pt^{300\,nm}$ samples. Sample size is given in mm ×mm and the ratio between directly heated area and radiating area is depicted for several samples with different size $r_A = A_{heat}/A_{radiation}$.

actual temperature in the sample. Namely, thermal radiation and heat transfer from heating source to the thin film. In vacuum environment, thermal radiation of the sample surface is dominant and quantified by the emission power P_ϵ depending on the temperature to the power of 4, the emissivity ϵ of the material and the emitting surface area A. A disparity of T_{cal} between different sized samples is identified and can at first glance be ascribed to the overlap of the sample over the heating stripe as indicated by the sketch in Fig. 3. Since the sample width increases, whilst the width of direct contact to the 10 mm wide heating stripe is constant, the decisive parameter is the ratio of directly heated area and the radiating area ($r_A = A_{heat}/A_{radiation}$). We estimate the ratio by considering geometric surfaces. The respective ratio is given in the inset of Fig. 3. Another circumstance that effects the temperature in the sample is the roughness of both, the heating stripe and the substrate, as heat conductance may be altered due to cavities. Particularly, the heating stripe is not perfectly flat. The actual contact area can be different for every sample and even for a re-positioned sample. Especially at lower temperatures this might have an increased impact, as heat conductivity of the glass substrate is lower than at elevated temperatures. Nevertheless, calibration curves of two different 12 mm × 50 mm samples are in good agreement within the uncertainty.

The precision of the computed T_{cal} is indicated by the error bars Fig. 3. The uncertainty arises from two main sources: the calculated error in peak location during Le Bail refinement and due to possible systematic effects such as sample positioning or instrumental drift. And second, the precision of thermal expansion coefficient taken from Ref. [20]. Since no precision of the fit of $\alpha(T)$ in [20] is given, an estimation based on presented variance in Ref. [19] is done here. Assuming the reference temperature T_0 is precise, the uncertainty of T_{cal} is calculated by propagation through Eq. (1) and is of maximal magnitude ±10 K. While there remain inherent uncertainties due to potential deviation of thin film expansion in comparison to reference thermal expansion data, it provides a reliable local temperature determination. Moreover, the method ensures excellent reproducibility and spatial relevance, as it directly probes the temperature within the actual thin film stack under investigation and is invariant to sample geometry and emissivity. All

the discussed facts emphasize the necessity of an in-situ calibration for thin film applications when a measurement stage with a heating stripe is used. With our presented technique, neither the knowledge of exact sample size (i.e. radiating surface area), nor the exact position of the sample with regards to heating stripe is mandatory. It is of major importance when the surface of the thin film has micro or even nano structured features and an exact determination of the surface area is hardly feasible. In particular, emissivity can be very sensible to surface characteristics. An ex-situ temperature calibration can easily be misinterpreted or even become invalid.

3.2. Crystallization of TiO_{2-x} based thin films

SEM images of the temperature treated TiO_{2-x} layer on top of the Pt layer are shown in Fig. 4. The thin films are removed from the glass substrate by a lift-off preparation, in order to reduce charging effects and to enhance image quality. The images illustrate the rough substrate and the coverage of the TiO_{2-x} thin films and give a visual impression of its microstructure. We note that substrate surface roughness can influence the mechanical coupling at the film–substrate interface, particularly in high-temperature environments. In our experiments, a moderately increased surface roughness reduces coherent in-plane strain transfer by disrupting the continuity of the interface, which facilitates partial mechanical decoupling. This promotes stress relaxation in both the Pt calibration layer and the TiO_2 film, helping to minimize thermal mismatch effects. While increased roughness may improve local adhesion through mechanical interlocking, it simultaneously decreases the lateral coherence of stress propagation, which is beneficial for isolating thermal expansion behavior of the Pt layer. Moreover, the GI-XRD geometry ensures that the measured out-of-plane lattice parameters are less sensitive to in-plane constraints and local variations in morphology, such as the irregular film topography seen in Fig. 4.

In Fig. 5, we reveal XRD patterns recorded at RT after the HT program of samples deposited from different M:TiO_2 (M=Nb, Ti) targets with 3% oxygen (a) and without adding oxygen (b). In all samples, irrespective of the metallic Nb or Ti particle content, single phase anatase structure is observed in the diffraction pattern when oxygen was present during the sputtering process. In contrast, oxygen free deposition leads to a mixture of rutile, anatase, and brookite phase, with only one exception, the ^{0}TO-0 sample, where we observe also single phase anatase. For Le Bail refinement, initial CIF from ISCD 9852 [22], ICSD 9161 [23] and ICSD 36 408 [24] are employed for anatase, rutile, and brookite, respectively. Lattice parameters a, b, and c, domain size D, and microstrain v are extracted for the three polymorph phases and listed in Table 3. Notice, that an insignificant microstrain as well as a domain size larger than the resolution limit (about 130 nm) of the XRD system are denoted as N/A.

First, we focus on Nb doped samples with oxygen containing conditions, as shown in Fig. 5 (a). The fact that there is no evidence of any metallic niobium or niobium-oxide phases demonstrates substitution of Ti by Nb in the lattice of anatase. However, we observe shifted anatase reflex positions to smaller diffraction angles for increasing Nb content. This impression can be verified by slightly increased lattice parameters. For undoped anatase, an average lattice constant $a = b = 3.793$ Å and $c = 9.522$ Å are calculated, which is in good agreement with the used CIF [22]. In Fig. 6 (a) we see that lattice parameters increase almost linearly with Nb content, whereas c of the ^{10}NTO-3 sample deviates from this trend ($c = 9.617$ Å). This outlier can also be seen in Fig. 6 (b), where the lattice parameters are presented in dependence on oxygen flow. For the 3% sample, c is significantly higher, while values at lower oxygen flow are comparable.

Generally, the lattice expansion is likely caused by a slightly larger ionic radius of niobium (0.61 Å for Ti^{4+} and 0.64 Å for Nb^{5+} [25]). However, this is not the only mechanism which has to be considered. In [26], first principle calculations are reported and it is shown that the change in lattice size for Nb doped anatase is affected by the presence of oxygen vacancies (V_O) or oxygen interstitials (O_i). A lattice with only Nb on a Ti site (Nb_{Ti}) shows an enlargement of a, whereas shrinking of c is calculated. In contrast, when Nb_{Ti} is combined with V_O (Nb_{Ti}-V_O) or O_i (Nb_{Ti}-O_i), both a and c increase. The elongation of c is significantly stronger in the case of Nb_{Ti}-O_i compared to Nb_{Ti}-V_O. This aligns in good agreement with our observation. Therefore, we suggest that, in the case of the 3% samples, oxygen excess conditions prevail, favoring the formation of oxygen interstitials. And at lower oxygen flow, there is oxygen deficiency and oxygen vacancies are present.

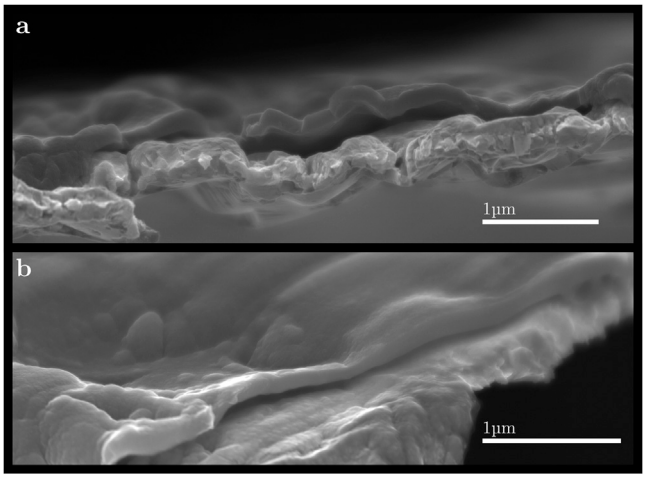

Fig. 4. SEM images of a Nb:TiO_{2-x} layer on a Pt thin film after a lift-off preparation.

We determine reasonable small values of microstrain, comparable to literature values of TiO_2 thin films [27]. This supports the hypothesis that defects, such as O_i, V_O and Nb_{Ti}, are compensated by the change in lattice parameters. It is worth mentioning, that as Nb content increases, the domain size also grows. This trend contrasts with the behavior reported in thin films prepared by sol–gel method in [28], where an opposite progress is observed, accompanied by strongly elevated strain. We do not perceive any indication of higher microstrain due to Nb doping. Notably, we identify larger anatase domain sizes at lower oxygen flow rates, suggesting that growth is favored under slightly oxygen deficient conditions. A potential explanation is given by [29], as oxygen vacancies can serve as active sites for diffusion and hence, may enhance growth kinetics.

The situation is not entirely clear for the samples prepared without oxygen, where we identify mixed polymorphic phases, as Le Bail refinement confirms the presence of anatase, rutile and brookite. However, due to significantly lower intensities and overlapping peaks, the parameters extracted from Le Bail fits are subject to larger uncertainties. We qualitatively recognize the trend that the intensity ratio of anatase 101 to rutile 110 decreases with increasing Nb or Ti content in the target. Rutile phase is characterized by rather small domain sizes in the range 52 Å to 74 Å and hence, poor crystalline quality is indicated. On the other hand brookite phase exhibits larger domain sizes up to 1214 Å (for the ^{5}NTO-0) with insignificant microstrain. For the ^{10}NTO-0 and ^{19}TO-0, the anatase/brookite intensity is hardly present anymore. Therefore, only the rutile phase has reliable results from Le Bail refinements.

The situation is very complex, because the interaction between potential defects such as Ti interstitials (Ti_i), O_i, V_O and Nb_{Ti} strongly depend on the respective defect density. Further, the interaction is different for each of the three polymorphic phases. Therefore, the interpretation cannot be further clarified without quantified investigation of potential defects and defect densities, which exceeds the scope of this work. Nevertheless, our observations suggest a more impeded and defect-rich integration of Nb due to the absence of oxygen during the deposition process.

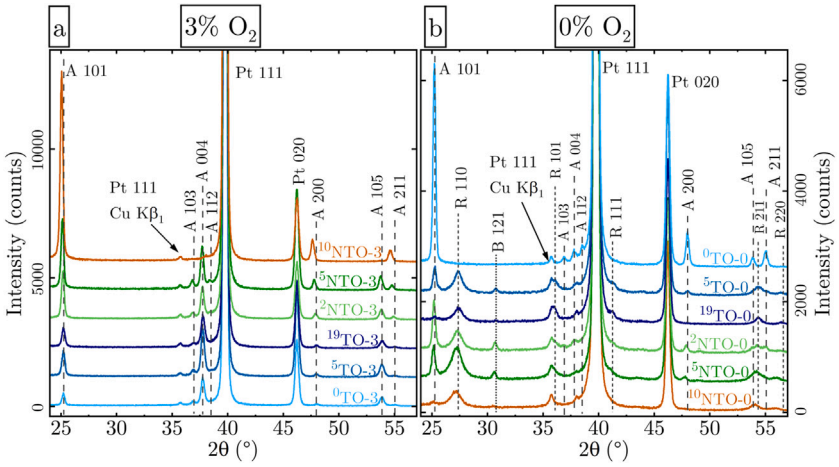

Fig. 5. XRD pattern of thin films prepared from different M:TiO_{2-x} targets (M=Nb,Ti) with (a) $\mathcal{F}_{O_2} = 3\%$ and (b) without addition of oxygen to the process gas ($\mathcal{F}_{O_2} = 0\%$). Patterns are shifted by a constant value of intensity for better visibility; for the same reason, the arrangement of different patterns is switched for (a) and (b).

Table 3
Summarized XRF and XRD results.

Sample	*h* nm	*R* nm/min	[Nb] at%	Phase	a Å	b Å	c Å	*D* Å	*v* %	T_{onset} K
^{0}TO-3	141	0.5	0	Anatase		3.793	9.522	330	0.14	529
^{0}TO-0	146	3.7	0	Anatase		3.792	9.522	1115	0.17	525
^{5}TO-3	142	0.5	0	Anatase		3.794	9.522	423	0.22	525
^{5}TO-0	138	4.6	0	Anatase		3.789	9.615	381	N/A	520
				Brookite	9.155	5.480	5.158	805	N/A	
				Rutile		4.607	2.962	74	N/A	531
^{19}TO-3	142	0.6	0	Anatase		3.794	9.519	345	0.23	530
^{19}TO-0	135	5.4	0	Rutile		4.600	2.959	66	N/A	729
^{2}NTO-3	131	0.9	1.24	Anatase		3.802	9.529	582	0.22	528
^{2}NTO-0	139	6.0	1.31	Anatase		3.800	9.526	413	N/A	530
				Brookite	9.146	5.500	5.154	401	N/A	
				Rutile		4.614	2.911	53	N/A	547
^{5}NTO-3	146	1.2	2.92	Anatase		3.808	9.534	717	0.16	562
^{5}NTO-0	135	7.1	3.06	Anatase		3.809	9.505	792	0.5	543
				Brookite	9.192	5.506	5.146	1214	N/A	
				Rutile		4.629	2.928	52	N/A	598
^{10}NTO-3	147	1.6	5.86	Anatase		3.817	9.617	822	0.16	617
^{10}NTO-1	127	3.6	6.46	Anatase		3.823	9.537	1190	0.22	664
^{10}NTO-0.6	157	6.0	6.59	Anatase		3.826	9.544	N/A	0.16	663
^{10}NTO-0.4	143	7.2	6.45	Anatase		3.822	9.544	N/A	0.15	633
^{10}NTO-0.2	139	8.2	6.52	Anatase		3.831	9.551	N/A	0.11	637
^{10}NTO-0	127	10.6	5.76	Rutile		4.639	2.919	61	N/A	615

Continuing with the temperature development of crystal structure, in Fig. 7, XRD patterns recorded from RT to 1273 K (nominal temperature) are presented for ^{5}NTO samples with 0% (a) respective 3% (b) oxygen as examples. The patterns at RT (299 K) are recorded after the heating cycle. As-deposited TiO_{2-x} based thin films did not show any crystalline features in the XRD pattern (not shown). Le Bail refinement was again applied to determine lattice parameter *a* of Pt for each temperature step and sample. Following the procedure described in Sections 2.2 and 3.1, the temperature is calibrated for each sample individually. We determined integrated peak intensities of anatase 101 (for the 3% oxygen samples) and rutile 110 (for the oxygen free deposition). Additionally we investigated the anatase 101 respective brookite 021 and the brookite 121 region in the 0% case. To assess crystallization onset temperature (T_{onset}), integrated anatase 101 peak intensities are plotted against their respective calibrated temperature in Fig. 8 for different Nb content (a) and the oxygen variation (b). T_{onset} is identified by the intersection of a linear fit in the region of crystallization and the baseline. The extrapolated onset temperatures, indicating crystallization temperature, are summarized in Table 3 for all investigated samples. Generally, we observe elevated crystallization onset temperatures for anatase with increasing Nb content. In contrast, for the pure TiO_{2-x} films the onset temperature is in the range 525 K to 530 K, regardless of the Ti composite content in the target. This is in good agreement with reported values, for example in [30] for films with similar thickness. Taking a look at the oxygen variation (see Fig. 8 b), we recognize similar anatase onset temperature for 0.2% and 0.4% and slightly elevated temperatures for 0.6% and 1%, and further a lower one for 3%. In Fig. 9 the relevant XRD patterns at RT (after temperature program) for ^{10}NTO samples deposited with different amount of oxygen are presented. The sample without oxygen is the only one where rutile phase is present. An oxygen flow of 0.2% during the sputter process is sufficient to produce a pure phase polycrystalline anatase thin film via post deposition annealing in vacuum. Generally, it is understood that the resulting phase depends on the particle energy during sputtering, which can be controlled by total pressure, sputter gas species or substrate bias and temperature [31,32]. However the key factor to tailor the growth of a specific phase is still not clear [33]. In our study, anatase phase is stable at all investigated

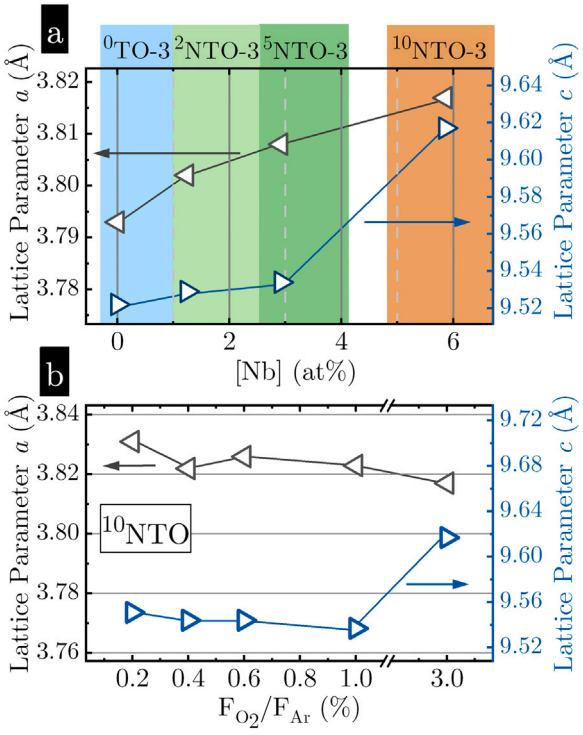

Fig. 6. Anatase lattice parameter *a* and *c*, extracted from Le Bail refinement presented in dependence on atomic niobium percentage (a) and on oxygen flow in the ^{10}NTO samples (b). The symbols are connected with lines for guidance of eyes.

temperatures. When we compare the pattern for different oxygen content, we notice a significantly elevated intensity for the anatase 101 reflex and disappeared 103, 004, 112 and 105 reflection in the case of ^{10}NTO-3 sample, indicating a crystallization in preferential orientation. A potentially higher sputter energy due to an enhanced presence of high energetic oxygen anions, could be an explanation for a different crystallization kinetic [33]. Here we want to point out again that the reflection at around 37.9° in Fig. 9 is the tungsten Lα_1 wavelength position of the Pt 111 plane and is not the anatase 112 reflection. Onset temperatures for anatase 101/brookite 021 and brookite 121 coincide. Therefore, it is not possible to distinguish between anatase and brookite onset in the case of oxygen free deposition. Again, similar to lattice parameter extraction, for the ^{10}NTO-0 and ^{19}TO-0 anatase/brookite intensities are too low for a reliable onset determination.

3.3. Opto-electrical properties of ^{10}NTO based thin films

In this section we focus on opto-electrical properties of ^{10}NTO thin films prepared with varying oxygen flow during deposition. We link them to the findings of structural analysis presented in the previous Section 3.2. In Table 3, the Nb content and film thickness *h*, measured by WD-XRF, and the resulting effective deposition rate R_{eff} are given. We trace comparable Nb content between 6.45at% to 6.59at% for the ^{10}NTO samples deposited with an oxygen flow between 0.2% to 1%. The Nb percentage decreases for the sample without oxygen in the process gas to 5.76at%. Additionally, a lower oxygen to metal ratio and an elevated Ti content is observed in comparison to deposition with oxygen. For the 3% sample, we also have a reduced Nb content of 5.86at%. This might be explained by a different effect of oxygen on the sputter yield of Nb and TiO_{2-x}. Regarding the deposition rate, we want to emphasize, that we used a sample holder which allows simultaneous deposition of four samples. Substrate movement is optimized to achieve homogeneous and fully covered films on rough substrates, even for low film thicknesses of a few tenth of nm, at the cost of deposition rate. Experiments comparing stationary rotating deposition with planetary movement reveal a higher rate by a factor 2.8. Using this factor leads to a gross deposition rate of almost 23 nm/min for the ^{10}NTO-0.2 sample.

It is well known that Nb dopant concentration or more general, defect densities, are decisive for opto-electrical properties, e.g. resistivity (ρ), charge carrier density (n_e), electron mobility (μ_e) and absorption behavior. For the application as a TCO, low absorption has to be accompanied with high conductivity. In Fig. 10a, absorption determined by transmission/reflection measurements is presented for ^{10}NTO samples with different oxygen flow before and after vacuum annealing. Before tempering, samples prepared with an oxygen flow of 0.6 % or higher manifest only minor absorption in the investigated spectral range below bandgap energy. For the ^{10}NTO-0.4 sample, we observe slightly increased absorption in the visible (VIS) range extending into the near infra-red (NIR). ^{10}NTO-0.2 and ^{10}NTO-0, in contrast, show significant defect absorption peaking in the VIS. After annealing, we generally observe enhanced absorption, particularly in the IR, indicating free charge carrier or Drude like absorption. In ^{10}NTO-0.2, free charge carrier absorption is superimposed with defect absorption, which is dominating the spectrum. The oxygen free deposition, in contrast, shows rather only defect absorption. An enlarged view on the absorption in the bandgap region (in Fig. 10b) shows a flat and curved absorption onset in ^{10}NTO-0.2 after vacuum annealing, however, with a distinctive blue shift of the band edge in comparison to the other samples.

To quantify the phenomenologic observations, optical data from transmission/reflection and spectroscopic ellipsometry were evaluated simultaneously using RIG-VM code developed at Fraunhofer IST [34]. The dielectric function is modeled with four Tauc–Lorentz oscillators. Two were used for the bandgap absorption, one for sub-bandgap or tail absorption and one for defects when necessary. If applicable, an additional Drude term was used to model free charge carrier absorption. The resulting fits can be seen in the supplementary. In Fig. 10c we present the calculated absorption coefficients α in Tauc plots assuming an indirect transition. E_g is determined by an extrapolated linear fit in the region where Tauc relation is valid and its intersection with the *x*-axis. The values are summarized in the inset. In a previous work [9], we reported bandgap energies of 3.28 eV and 3.38 eV for undoped TiO_{2-x} thin films (before annealing) prepared with and without oxygen, respectively. In comparison, slightly higher values of 3.38 eV for ^{10}NTO-0 and 3.41 eV for ^{10}NTO-3 are observed in this study after vacuum annealing. Samples with an oxygen flow between 0.4% to 3% show similar bandgap energies in the range from 3.40 eV to 3.44 eV. However, a more curved behavior is recognized in the onset region for the ^{10}NTO-0.4 and ^{10}NTO-3 samples, indicating increased density of tail states. We address the presence of tail states to the formation of oxygen interstitials indicated by XRD in ^{10}NTO-3. In case of ^{10}NTO-0.4, an increased number of oxygen vacancies is likely responsible for tail absorption. In contrast,^{10}NTO-0.6 and ^{10}NTO-1 show a rather sharp rise with a steep slope, indicating a clean band edge and a low degree of structural disorder or defects. The ^{10}NTO-0.2 sample exhibits distinct characteristics, with a significantly higher band gap energy of 3.56 eV. Although its crystal structure and Nb percentage are very similar to those of ^{10}NTO-0.4, ^{10}NTO-0.6, and ^{10}NTO-1, its conductivity is markedly improved, as shown in Fig. 11 and discussed below. Therefore, we attribute the increased band gap energy to a Moss–Burstein shift [35,36], which is an indicator that this sample is a degenerated semiconductor. In Fig. 10c, two linear regions are visible around the potential onset points for the ^{10}NTO-0.2 sample, complicating a precise evaluation of the bandgap. As a result, only bounds can be established, with the upper bound indicated above at 3.56 eV (dashed line) and the lower bound extrapolated at 3.19 eV (dotted line). The shallow slope of the lower bounds deduces a less clean edge, due to a high density of defect states on a broader energetic distribution.

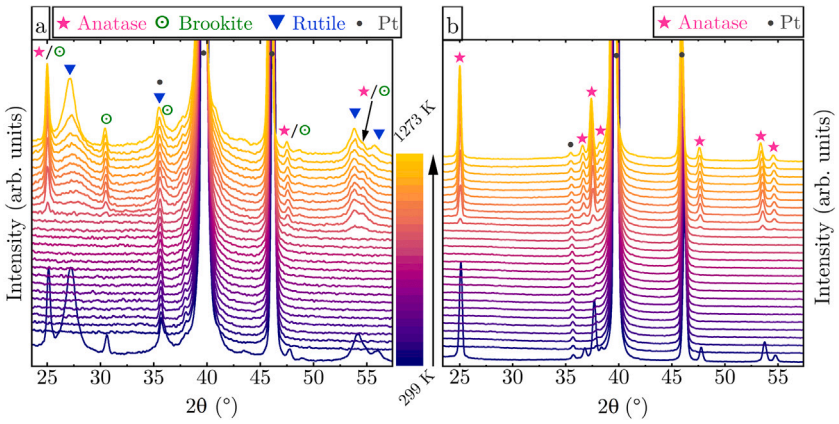

Fig. 7. Temperature evolution of XRD patterns of (a)^{5}NTO-0 and (b)^{5}NTO-3. Bottom lines represent room temperature patterns after heat treatment.

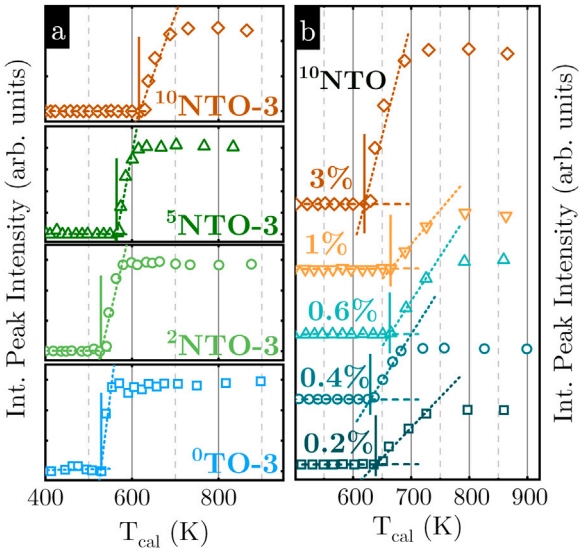

Fig. 8. Integrated peak intensities of anatase 101 reflex dependent on calibrated temperature for target variation (a) and oxygen flow variation (b). Dashed lines represent linear fits of respective base line and crystallization region. Crystallization onset temperatures are indicated by vertical lines.

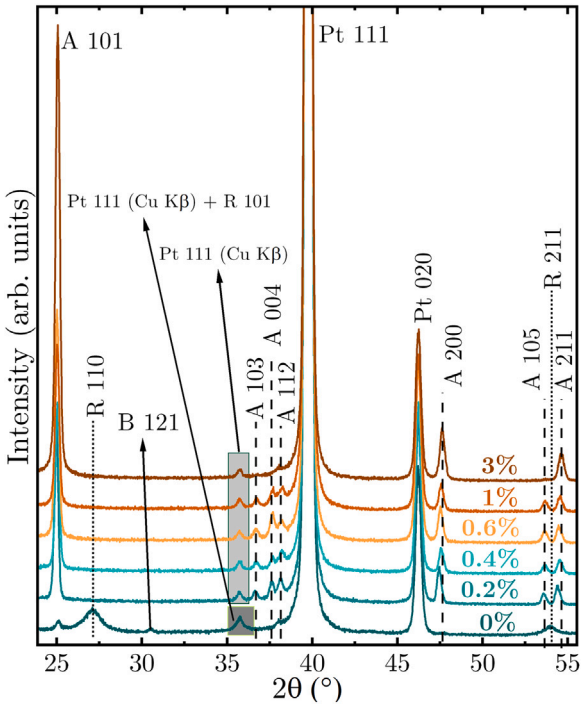

Fig. 9. XRD patterns after vacuum annealing for different oxygen flow during deposition using ^{10}NTO target.

In Fig. 11, the resistivity ρ after the vacuum HT program is shown for different oxygen flow. The behavior is not intuitively clear and each data point is discussed in the following. The sample without oxygen flow (^{10}NTO-0) shows a relatively high value of $\rho = 76\,\mathrm{m\Omega\,cm}$. This can be primarily attributed to the presence of rutile phase, which has a higher effective electron mass $m^*_{\mathrm{rutile}} \sim 20\,m_0$ [37] (m_0 is the free electron mass) in comparison to anatase $m^*_{\mathrm{anatase}} \sim 1\,m_0$ [38], resulting in a lower electron mobility. Hall measurements suggest a rather low mobility of $3 \times 10^{-2}\,\mathrm{cm^2\,V^{-1}\,s^{-1}}$, however, charge carrier density is notable high with $3.8 \times 10^{21}\,\mathrm{cm^{-3}}$. Besides the enhanced effective electron mass in rutile, we relate the low mobility to a high concentration of defects, acting as scattering centers. Poor crystallinity was depicted for this sample (see Section 3.2) from which one can deduce a high defect concentration (e.g. Ti or Nb interstitials), which aligns well with enhanced defect absorption. For an oxygen flow of 0.2%, we observe lowest resistivity $\rho = 1.2\,\mathrm{m\Omega\,cm}$ at the ^{10}NTO-0.4 sample, indicating donor like defect states. Hall measurements reveal a charge carrier density of $2.6 \times 10^{21}\,\mathrm{cm^{-3}}$ and a mobility of about $2\,\mathrm{cm^2\,V^{-1}\,s^{-1}}$. Increasing the oxygen flow results in enhanced resistivity, i.e. $14.3\,\mathrm{m\Omega\,cm}$ for ^{10}NTO-0.4 and as high as $127\,\Omega\,\mathrm{cm}$ for ^{10}NTO-1. A lower number of donor-like defects is anticipated to contribute to the reduced conductivity. However, due to an unstable and not reproducible Hall voltage, reliable results could not be obtained to confirm the decreased charge carrier density. In contrast to the monotony increasing resistivity for ^{10}NTO-0.2 till ^{10}NTO-1, a certain drop of resistivity is observed for the ^{10}NTO-3 sample. XRD results indicate the formation of oxygen interstitials in ^{10}NTO-3, favored in oxygen rich conditions, which act as electron traps and compensate excess electrons introduced by the Nb^{5+} [39]. The lower resistivity in comparison to ^{10}NTO-1 might be explained by an enhanced mobility, due to its crystallographic properties. This can be correlated to the observed reduction in crystallization onset temperature, indicating different growth kinetics. A strong preferential growth with increased overall intensity in XRD analysis could be a potential origin of enhanced mobility. But, also for this sample, Hall measurements were not possible due to a fluctuating contact resistance. We address the problems to an increased resistivity at the surface due to longer exposure to air during shipping to and storage at the location of measurement. Nevertheless, a slightly steeper raise of the Drude absorption indicate an enhanced mobility.

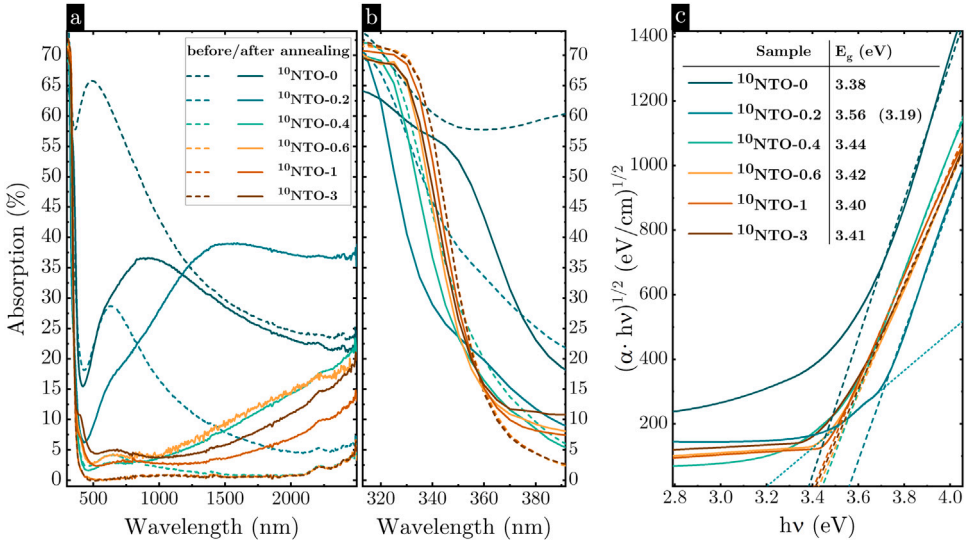

Fig. 10. (a) Absorption A for oxygen flow variation before and after vacuum annealing, calculated from transmission/reflection (T/R) experiments by $A = 100 - R - T$. (b) enlarged view on band gap absorption (identical scale on y-axis as in (a)). (c) Tauc-plot for oxygen flow variation, using calculated absorption coefficients by modeling the dielectric function. Determined optical bandgap energies are presented in the inset. (For interpretation of the references to color in this figure legend, the reader is referred to the web version of this article.)

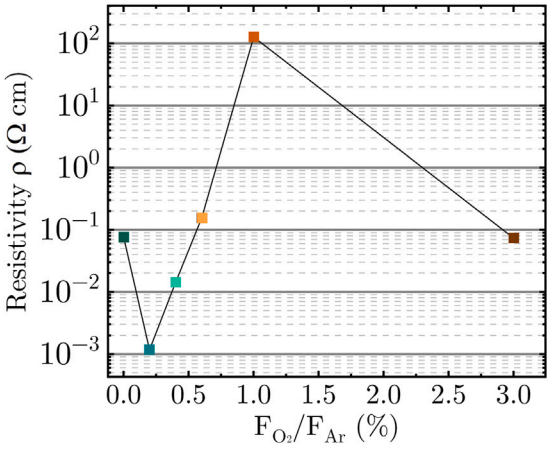

Fig. 11. Specific resistivity for ^{10}NTO samples prepared with different oxygen flow during deposition. Data points are connected with lines for eye guidance.

Oxygen vacancies are often correlated to enhanced charge carrier densities and conductivity [16,40]. On the other hand, high crystalline quality is reported to be decisive for elevated mobility [41]. High mobility and conductivity is reported for films by pulsed laser deposition (PLD). Epitaxial growth on single crystal substrates, resulting in preferential 004 orientation yields a mobility in the range of 16 $cm^2\ V^{-1}\ s^{-1}$ to 30 $cm^2\ V^{-1}\ s^{-1}$ and resistivity between $2 \times 10^{-4}\ \Omega$ cm to $3 \times 10^{-4}\ \Omega$ cm (at room temperature) depending on the Nb concentration [42]. However, it is not clarified whether the orientation or a high crystal quality is responsible for the mobility. PLD deposited NTO films on glass with post deposition treatment reach resistivity as low as $4.6 \times 10^{-4}\ \Omega$ cm for hydrogen annealing and $7.8 \times 10^{-4}\ \Omega$ cm for vacuum annealing [43]. For RF sputtered NTO films on heated single crystal substrates resistivity of $3.3 \times 10^{-4}\ \Omega$ cm, a carrier concentration of $2.4 \times 10^{21}\ cm^{-3}$ and a mobility of 7.6 $cm^2\ V^{-1}\ s^{-1}$ with a strong correlation to the intensity of anatase 004 reflection is reported [44]. As a matter of fact, there is a competitive interplay between high carrier concentration induced by defects (oxygen vacancies or Nb dopants) and high electron mobility requiring low density of scattering centers. For example, in [42] it is reported that charge carrier density is increased almost linearly with Nb content, while electron mobility shows a maximum at lower doping concentration. Compared to values in literature, ^{10}NTO-0.2 demonstrates, that DC sputtered thin films have the potential to compete with other deposition techniques.

4. Summary, conclusion and outlook

We performed in-situ temperature calibration in high-temperature XRD experiments conducted in high vacuum, using a crystalline Pt thin films as calibration standard. The calibration was then applied to TiO_2 based thin films deposited on the Pt coated fused silica substrates. The results identify and emphasize substantial discrepancy of the real sample temperature from the nominal set temperature, presumably connected to radiation losses at the surface. Our calibration technique enables precise thermal XRD analysis with an uncertainty less than 10 K and therefore, a more accurate assessment of crystallization onset temperature is feasible. We presented crystallization onset temperatures for various deposition conditions of pristine and Nb doped TiO_{2-x} thin films. The knowledge of crystallization onset temperature for a wide range of process conditions (including target variation) is essential for process development with desired properties. In a next development step, our technique can be used to study the thermal expansion behavior of the investigated thin film. Once it is known, the calibration can also be performed with the reflection peaks of the actual sample without the Pt layer.

Analyzing crystal structure and correlated material properties (i.e. opto-electronic), reveals a high sensibility to the oxygen flow during the deposition. This demonstrates the potential of controlled tuning of properties with the described deposition process. Especially, the formation of pure anatase phase by adding minimal amount of oxygen to the process gas can be used on purpose, if needed. DC sputtered TiO_2 based thin films from metal–ceramic composite targets bring extensive advantages in comparison to commonly used reactive sputtering from metallic targets. The hysteresis effect is expected to be not present significantly, as low oxygen flow allows deposition in a quasi-metallic mode, while still being able to produce near stoichiometric and highly transparent material. Process control is easier and therefore, stable process conditions can be achieved with less effort and its scalability is preserved. With view on industrial application, the investment is lower and the energy efficiency is enhanced in comparison to RF sputter-mode. We demonstrated a possible process window resulting

in considerable conductivity with reasonable deposition rate. Indeed, for PLD deposited Nb:TiO_2 films, lower resistivity is reported. PLD is a highly precise technique, which allows high quality and control of stoichiometry. However, PLD has typically low deposition rates and achieving uniform thin films on a large scale is very challenging. Therefore, it is not an appropriate technique for industrial production with high throughput. We would like to emphasize that this study does not focus on process optimization for achieving the best performance as a TCO. Fine-tuning the oxygen flow or optimizing the annealing process are clear avenues for further improvement. Regardless, the results of this work highlight the potential and provide a strong foundation for future work.

CRediT authorship contribution statement

David Freudenblum: Writing – original draft, Visualization, Project administration, Methodology, Investigation, Data curation, Conceptualization. **Gaston Gruber:** Writing – review & editing, Data curation. **René Schwiddessen:** Writing – review & editing, Data curation. **Florian Ruske:** Writing – review & editing, Investigation, Data curation. **Nikolaus Weinberger:** Writing – review & editing, Supervision, Resources.

Declaration of competing interest

The authors declare that they have no known competing financial interests or personal relationships that could have appeared to influence the work reported in this paper.

Acknowledgments

The work is part of the Project SolMates funded by the European Union (Project Nr. 101122288). D. Freudenblum is thankful to Nikolai Kraus for all the technical support and for reviewing.

Appendix A. Supplementary data

Supplementary material related to this article can be found online at https://doi.org/10.1016/j.jallcom.2025.181844.

References

[1] A. Drews, Calibration of a high temperature X-ray diffraction stage by differential thermal expansion, Adv. X- Ray Anal. 44 (2001).
[2] N.E. Brown, S.M. Swapp, C.L. Bennett, A. Navrotsky, High-temperature X-ray diffraction: solutions to uncertainties in temperature and sample position, J. Appl. Crystallogr. 26 (1) (1993) 77–81, http://dx.doi.org/10.1107/S002188989200877X.
[3] N. Weinberger, T. Kodalle, T. Bertram, R. Gunder, A. Saxer, R. Lackner, G.N. Strauss, C.A. Kaufmann, Phase development in $RbInSe_2$ thin films – a temperature series, Scr. Mater. 202 (2021) 113999, http://dx.doi.org/10.1016/j.scriptamat.2021.113999.
[4] A. Fujishima, T.N. Rao, D.A. Tryk, Titanium dioxide photocatalysis, J. Photochem. Photobiol. C: Photochem. Rev. 1 (1) (2000) 1–21, http://dx.doi.org/10.1016/S1389-5567(00)00002-2.
[5] J.M. Ribeiro, F.C. Correia, F.J. Rodrigues, J.S. Reparaz, A.R. Goñi, C.J. Tavares, Transparent niobium-doped titanium dioxide thin films with high seebeck coefficient for thermoelectric applications, Surf. Coat. Technol. 425 (2021) 127724, http://dx.doi.org/10.1016/j.surfcoat.2021.127724.
[6] Y. Lv, B. Cai, Q. Ma, Z. Wang, J.J. Liu, W.-H. Zhang, Highly crystalline Nb-doped TiO_2 nanospindles as superior electron transporting materials for high-performance planar structured perovskite solar cells, RSC Adv. 8 (37) (2018) 20982–20989, http://dx.doi.org/10.1039/c8ra03559h.
[7] C. Zhen, T. Wu, R. Chen, L. Wang, G. Liu, H.-M. Cheng, Strategies for modifying TiO_2 based electron transport layers to boost perovskite solar cells, ACS Sustain. Chem. Eng. 7 (5) (2019) 4586–4618, http://dx.doi.org/10.1021/acssuschemeng.8b06580.
[8] M.M. Tavakoli, P. Yadav, R. Tavakoli, J. Kong, Surface engineering of TiO_2 ETL for highly efficient and hysteresis–less planar perovskite solar cell (21.4%) with enhanced open–circuit voltage and stability, Adv. Energy Mater. 8 (23) (2018) http://dx.doi.org/10.1002/aenm.201800794.
[9] D. Stock, N. Weinberger, F. Ruske, L. Haug, M. Harnisch, R. Lackner, Development of direct current magnetron sputtered TiO_{2-x} thin films as buffer layers for copper indium gallium diselenide based solar cells, Thin Solid Films 786 (2023) 140115, http://dx.doi.org/10.1016/j.tsf.2023.140115.
[10] G.S. Park, S. Lee, D.-S. Kim, S.Y. Park, J.H. Koh, H. Da Won, P. Lee, Y.R. Do, B.K. Min, Amorphous TiO_2 passivating contacts for $Cu(In,Ga)(S,Se)_2$ ultrathin solar cells: Defect–state–mediated hole conduction, Adv. Energy Mater. 13 (8) (2023) http://dx.doi.org/10.1002/aenm.202203183.
[11] Y. Furubayashi, T. Hitosugi, Y. Yamamoto, K. Inaba, G. Kinoda, Y. Hirose, T. Shimada, T. Hasegawa, A transparent metal: Nb-doped anatase TiO_2, Appl. Phys. Lett. 86 (25) (2005) http://dx.doi.org/10.1063/1.1949728.
[12] H. Poelman, H. Tomaszewski, D. Poelman, D. Depla, R. de Gryse, Effect of the oxygen deficiency of ceramic TiO_{2-x} targets on the deposition of TiO_2 thin films by DC magnetron sputtering, Surf. Interface Anal. 36 (8) (2004) 1167–1170, http://dx.doi.org/10.1002/sia.1867.
[13] H. Baránková, S. Berg, P. Carlsson, C. Nender, Hysteresis effects in the sputtering process using two reactive gases, Thin Solid Films 260 (2) (1995) 181–186, http://dx.doi.org/10.1016/0040-6090(94)06501-2.
[14] K. Strijckmans, R. Schelfhout, D. Depla, Tutorial: Hysteresis during the reactive magnetron sputtering process, J. Appl. Phys. 124 (24) (2018) http://dx.doi.org/10.1063/1.5042084.
[15] S. Berg, T. Nyberg, Fundamental understanding and modeling of reactive sputtering processes, Thin Solid Films 476 (2) (2005) 215–230, http://dx.doi.org/10.1016/j.tsf.2004.10.051.
[16] D. Dorow-Gerspach, M. Wuttig, Metal-like conductivity in undoped TiO_{2-x}: Understanding an unconventional transparent conducting oxide, Thin Solid Films 669 (2019) 1–7, http://dx.doi.org/10.1016/j.tsf.2018.10.026.
[17] S. Seeger, K. Ellmer, M. Weise, D. Gogova, D. Abou-Ras, R. Mientus, Reactive magnetron sputtering of Nb-doped TiO_2 films: Relationships between structure, composition and electrical properties, Thin Solid Films 605 (2016) 44–52, http://dx.doi.org/10.1016/j.tsf.2015.11.058.
[18] A. Le Bail, H. Duroy, J.L. Fourquet, Ab-initio structure determination of $LiSbWO_6$ by X-ray powder diffraction, Mater. Res. Bull. 23 (3) (1988) 447–452, http://dx.doi.org/10.1016/0025-5408(88)90019-0.
[19] R.K. Kirby, Platinum-A thermal expansion reference material, Int. J. Thermophys. 12 (4) (1991) 679–685, http://dx.doi.org/10.1007/BF00534223.
[20] J.W. Arblaster, Crystallographic properties of platinum new methodology and erratum, Platinum Met. Rev. 50 (3) (2006) 118–119, http://dx.doi.org/10.1595/147106706X129088.
[21] K.H. Hong, G.M. McNally, M. Coduri, J.P. Attfield, Synthesis, crystal structure, and magnetic properties of $MnFe_3O_5$, Z. Anorg. Allg. Chem. 642 (23) (2016) 1355–1358, http://dx.doi.org/10.1002/zaac.201600365.
[22] M. Horn, C.F. Schwerdtfeger, E.P. Meagher, Refinement of the structure of anatase at several temperatures*, Z. Krist. 136 (3–4) (1972) 273–281, http://dx.doi.org/10.1524/zkri.1972.136.3-4.273.
[23] W.H. Baur, A.A. Khan, Rutile-type compounds. IV. SiO_2, GeO_2 and a comparison with other rutile-type structures, Acta Crystallogr. Sect. B Struct. Crystallogr. Cryst. Chem. 27 (11) (1971) 2133–2139, http://dx.doi.org/10.1107/S0567740871005466.
[24] E.P. Meagher, G.A. Lager, Polyhedral thermal expansion in the TiO_2 polymorphs; refinement of the crystal structures of rutile and brookite at high temperature, Can. Miner. 17 (1) (1979) 77–85.
[25] R.D. Shannon, Revised effective ionic radii and systematic studies of interatomic distances in halides and chalcogenides, Acta Crystallogr. Sect. A 32 (5) (1976) 751–767, http://dx.doi.org/10.1107/S0567739476001551.
[26] H. Kamisaka, T. Hitosugi, T. Suenaga, T. Hasegawa, K. Yamashita, Density functional theory based first-principle calculation of nb-doped anatase TiO_2 and its interactions with oxygen vacancies and interstitial oxygen, J. Chem. Phys. 131 (3) (2009) 034702, http://dx.doi.org/10.1063/1.3157283.
[27] B. Karunagaran, R.T. Rajendra Kumar, V. Senthil Kumar, D. Mangalaraj, S. Narayandass, G. Mohan Rao, Structural characterization of DC magnetron-sputtered TiO_2 thin films using XRD and Raman scattering studies, Mater. Sci. Semicond. Process. 6 (5–6) (2003) 547–550, http://dx.doi.org/10.1016/j.mssp.2003.05.012.
[28] G.H.M. Gomes, M.A.M.L. de Jesus, A.S. Ferlauto, M.M. Viana, N.D.S. Mohallem, Characterization and application of niobium-doped titanium dioxide thin films prepared by sol–gel process, Appl. Phys. A 127 (8) (2021) http://dx.doi.org/10.1007/s00339-021-04781-6.
[29] D.A.H. Hanaor, C.C. Sorrell, Review of the anatase to rutile phase transformation, J. Mater. Sci. 46 (4) (2011) 855–874, http://dx.doi.org/10.1007/s10853-010-5113-0.
[30] R. Kužel, L. Nichtová, Z. Matěj, D. Heřman, J. Šícha, J. Musil, Study of crystallization of magnetron sputtered TiO 2 thin films by X-ray scattering, in: D.G.f. Kristallographie (Ed.), Tenth European Powder Diffraction Conference, Oldenbourg Wissenschaftsv, ISBN: 9783486992533, 2015, pp. 247–252, http://dx.doi.org/10.1524/9783486992540-039.
[31] P.K. Song, Y. Irie, Y. Sato, Y. Shigesato, Crystal structure and photocatalytic activity of TiO 2 films deposited by reactive sputtering using Ne, Ar, Kr, or Xe gases, Jpn. J. Appl. Phys. (ISSN: 0021-4922) 43 (No. 3A) (2004) L358–L361, http://dx.doi.org/10.1143/JJAP.43.L358.

[32] M. Yamagishi, S. Kuriki, P.K. Song, Y. Shigesato, Thin film TiO2 photocatalyst deposited by reactive magnetron sputtering, Thin Solid Films (ISSN: 00406090) 442 (1–2) (2003) 227–231, http://dx.doi.org/10.1016/S0040-6090(03)00987-8, PII: S0040609003009878.

[33] H. Kotake, J. Jia, S.-i. Nakamura, T. Okajima, Y. Shigesato, Tailoring the crystal structure of TiO2 thin films from the anatase to rutile phase, J. Vac. Sci. Technol. A: Vac. Surf. Films (2015).

[34] A. Pflug, V. Sittinger, F. Ruske, B. Szyszka, G. Dittmar, Optical characterization of aluminum-doped zinc oxide films by advanced dispersion theories, Thin Solid Films 455–456 (2004) 201–206, http://dx.doi.org/10.1016/j.tsf.2004.01.006.

[35] E. Burstein, Anomalous optical absorption limit in InSb, Phys. Rev. 93 (3) (1954) 632–633, http://dx.doi.org/10.1103/PhysRev.93.632.

[36] T.S. Moss, The interpretation of the properties of indium antimonide, Proc. Phys. Soc. Sect. B 67 (10) (1954) 775–782, http://dx.doi.org/10.1088/0370-1301/67/10/306.

[37] H.P.R. Frederikse, Recent studies on rutile (TiO_2), J. Appl. Phys. 32 (10) (1961) 2211–2215, http://dx.doi.org/10.1063/1.1777045.

[38] H. Tang, K. Prasad, R. Sanjinès, P.E. Schmid, F. Lévy, Electrical and optical properties of TiO_2 anatase thin films, J. Appl. Phys. 75 (4) (1994) 2042–2047, http://dx.doi.org/10.1063/1.356306.

[39] H. Nogawa, T. Hitosugi, A. Chikamatsu, S. Nakao, Y. Hirose, T. Shimada, H. Kumigashira, M. Oshima, T. Hasegawa, Carrier compensation by excess oxygen atoms in anatase $Ti_{0.94}Nb_{0.06}O_{2+\delta}$ epitaxial thin films, Jpn. J. Appl. Phys. 49 (4R) (2010) 041102, http://dx.doi.org/10.1143/JJAP.49.041102.

[40] A. Song, G. Cao, D. Zhu, B. Zhao, Z. Fu, S. Cao, Q. Wang, J. Hu, Influence of oxygen vacancies on atomic chemistry and transparent conductivity of Nb-Doped TiO_2 films, J. Electron. Mater. 51 (12) (2022) 6885–6893, http://dx.doi.org/10.1007/s11664-022-09917-9.

[41] L. Lu, M. Guo, S. Thornley, X. Han, J. Hu, M.J. Thwaites, G. Shao, Remote plasma sputtering deposited Nb-doped TiO_2 with remarkable transparent conductivity, Sol. Energy Mater. Sol. Cells 149 (2016) 310–319, http://dx.doi.org/10.1016/j.solmat.2016.01.040.

[42] Y. Furubayashi, T. Hitosugi, Y. Yamamoto, Y. Hirose, G. Kinoda, K. Inaba, T. Shimada, T. Hasegawa, Novel transparent conducting oxide: Anatase $Ti_{1-x}Nb_xO_2$, Thin Solid Films 496 (1) (2006) 157–159, http://dx.doi.org/10.1016/j.tsf.2005.08.245.

[43] T. Hitosugi, A. Ueda, S. Nakao, N. Yamada, Y. Furubayashi, Y. Hirose, T. Shimada, T. Hasegawa, Fabrication of highly conductive $Ti_{1-x}Nb_xO_2$ polycrystalline films on glass substrates via crystallization of amorphous phase grown by pulsed laser deposition, Appl. Phys. Lett. 90 (21) (2007) http://dx.doi.org/10.1063/1.2742310.

[44] M.A. Gillispie, M.F.A.M. van Hest, M.S. Dabney, J.D. Perkins, D.S. Ginley, Rf magnetron sputter deposition of transparent conducting Nb-doped TiO_2 films on $SrTiO_3$, J. Appl. Phys. 101 (3) (2007) http://dx.doi.org/10.1063/1.2434005.